

Hen 2–104: a close-up look at the Southern Crab[★]

M. Santander-García^{2,1}, R. L. M. Corradi^{2,1}, A. Mampaso¹, C. Morisset³, U. Munari⁴, M. Schirmer²,
B. Balick⁵, and M. Livio⁶

¹ Instituto de Astrofísica de Canarias, 38200 La Laguna, Tenerife, Spain
e-mail: [miguelsg;amr]@iac.es

² Isaac Newton Group of Telescopes, Ap. de Correos 321, 38700 Sta. Cruz de la Palma, Spain
e-mail: [msantander;rcorradi;mischa]@ing.iac.es

³ Instituto de Astronomía, Universidad Nacional Autónoma de México, México, D. F., México
e-mail: morisset@astrocu.unam.mx

⁴ INAF Osservatorio Astronomico di Padova, via dell'Osservatorio 8, 36012 Asiago (VI), Italy
e-mail: munari@pd.astro.it

⁵ Department of Astronomy, University of Washington, Seattle, Washington 98195-1580, USA
e-mail: balick@astro.washington.edu

⁶ Space Telescope Science Institute (STScI), 3700 San Martin Drive, Baltimore, MD 21218, USA
e-mail: mlivio@stsci.edu

Received 7 December 2007 / Accepted 25 February 2008

ABSTRACT

Aims. The kinematics, shaping, density distribution, expansion distance, and ionized mass of the nebula Hen 2–104, and the nature of its symbiotic Mira are investigated.

Methods. A combination of multi-epoch HST images and VLT integral field high-resolution spectroscopy is used to study the nebular dynamics both along the line of sight and in the plane of the sky. These observations enable a 3-D spatio-kinematical model of the nebula to be constructed, which, with the measurement of its apparent expansion in the plane of the sky over a period of 4 years, provides the expansion parallax for the nebula. The integral-field data featuring the [SII] $\lambda\lambda 671.7, 673.1$ emission line doublet provide a density map of the inner lobes of the nebula, which with the distance estimation provide a measurement of its ionized mass.

Results. We measure densities ranging from $n_e = 500$ to 1000 cm^{-3} in the inner lobes, and from 300 to 500 cm^{-3} in the outer lobes. We determine an expansion-parallax distance of $3.3 \pm 0.9 \text{ kpc}$ to Hen 2–104, which implies an unexpectedly large ionized mass for the nebula of approximately one tenth of a solar mass.

Key words. stars: binaries: symbiotic – ISM: planetary nebulae: general – ISM: kinematics and dynamics

1. Introduction

Symbiotic stars are valuable laboratories for studying the physics of a variety of astrophysical processes, such as mass transfer, accretion and outflow, thermonuclear runaways, photo-ionization and shock-ionization, and the physico-chemistry of gas and dust in complex environments containing both hot and cold stars.

The formation of the nebulae that surrounds some symbiotic stars, especially those containing a Mira variable, is one example of these complex interactions, and their study is crucial for understanding aspects of the mass-loss history and geometry from these systems. A small fraction of the Mira wind is believed to be accreted by the white dwarf companion (Kenyon & Webbink 1984), which results in quasi-stable thermonuclear burning at its surface (e.g. Sokoloski 2002) that sometimes ends in thermonuclear outbursts (e.g. Kenyon 1986; Livio et al. 1989) lasting for hundreds of years (e.g. Munari 1997). The fast winds from the

white dwarf collide with the slower, non-accreted Mira wind, and shape complex circum-binary nebulae. Currently, about a dozen of these nebulae have been optically resolved (Corradi 2003). Most of them show bipolar morphologies, similar to those of many planetary nebulae (PNe) and protoplanetary nebulae (PPNe) (Corradi & Schwarz 1995; Sahai 2002).

The distance of these systems is generally poorly known, despite it being a basic parameter to determine their overall physical properties, such as their total luminosities, the mass of their ejecta or their kinematical ages. The advent of high spatial-resolution instruments such as HST enables the problem to be faced by measuring the expansion-parallax of some of these nebulae. The procedure is to measure the growth of the nebula in the plane of the sky using multi-epoch imaging, and combining this information with the expansion velocity, once the Doppler shifts have been measured and deprojected according to the adopted 3-D morphology. It has been applied to several relatively close PNe (NGC 6543, Reed et al. 1999; IC 2448, NGC 6578, NGC 6884, NGC 3242 and NGC 6891, Palen et al. 2000) and to one symbiotic nebula (Hen 2-147, Santander-García et al. 2007a).

Named the Southern Crab after its resemblance to the legs and claws of that animal, the nebula around Hen 2–104 (also, PN G315.4+09.4, and V852 Cen) was discovered by

[★] Based on observations with the NASA/ESA Hubble Space Telescope, obtained at the Space Telescope Science Institute, which is operated by the Association of Universities for Research in Astronomy, Inc. under NASA contract No. NAS5-26555; and on observations obtained at the 4 m NTT and the 8 m VLT telescopes of the European Southern Observatory in Chile.

Schwarz et al. (1989). Although similar, in morphology and kinematics, to several bipolar planetary nebulae (Corradi & Schwarz 1993b), the system has been unequivocally recognized as a genuine symbiotic star after Whitelock (1987) detected a Mira in its core by means of long-term photometric monitoring. The dynamics of this magnificent nebula, which spans $70'' \times 35''$ in the plane of the sky, was studied by Corradi & Schwarz (1993a) and then analysed in great spatial and spectral detail by Corradi et al. (2001).

The distance to Hen 2–104 is controversial. While Wright and Allen (1978) found a distance of 7.92 kpc, Schwarz et al. (1989) estimated 0.8 kpc. Whitelock (1987) and then Corradi et al. (2001) used the Period–Luminosity relation for Mira stars to derive an intermediate distance of 4.7 kpc and 4.4 kpc, respectively.

In this paper, we present the results of the analysis of an NTT+SOFI NIR spectrum, integral-field high-resolution VLT spectra, as well as of an 2003 HST [NII] image of the nebula, which is compared to an image obtained on 1999. Using these data, we present the first spectroscopic detection of the Mira, the determination of the expansion parallax of the nebula, its density map, and an estimation of its ionized mass and total luminosity of the system.

2. Observations and data reduction

2.1. Imaging

Two sets of [NII] 658.3 nm images of Hen 2–104 were obtained using the Wide Field Planetary Camera 2 (WFPC2) on the Hubble Space Telescope (HST) on May 22, 1999 (programme GO7378) and May 10, 2003 (programme GO9336) respectively (see Fig. 1). Images from both epochs were obtained through the *F658N* filter (central wavelength/bandpass = 659.0/2.2 nm), which, assuming no significant degradation between epochs, transmits the [NII] line with 78% efficiency and the $H\alpha$ line with 1% efficiency at the heliocentric systemic velocity of Hen 2–104. An additional set of WFPC2 images was taken on May 20, 2001 (programme GO9050), using the *F656N* filter (central wavelength/bandpass = 656.4/2.2 nm). In this case, the transmission efficiency was 78% in $H\alpha$, 11% in [NII] 654.8 and 6% in [NII] 658.3.

We computed the observed total fluxes from the nebula in both $H\alpha$ and [NII] 658.3 nm, following the procedure described by Luridiana et al. (2003). After subtraction of the central unresolved core and decontamination from continuum and neighbour emission lines, the observed total fluxes from the nebula were estimated to be 3.6×10^{-12} in $H\alpha$ and 2.1×10^{-12} erg cm⁻² s⁻¹ in [NII] 658.3 nm. These are consistent with the values given by Shaw & Kaler (1989) for a 10'' diameter aperture centered on the star.

The HST images (one dataset per epoch) were obtained using a 4-point dithering pattern to properly sample the HST point spread function (PSF). They were then reduced using the “multidrizzle package” (Koekemoer et al. 2002), an automated dithered image combination and cleaning task in PyRAF (Python IRAF). This routine first creates a bad-pixel mask using calibration reference files, and performs the sky subtraction. Next, the software arranges the four WFPC2 CCDs into a mosaic, where geometric distortion effects are corrected, including time-dependent distortions due to CCD rotations and flexure. Then it removes cosmic rays and creates, for each epoch, a combined and drizzled image with a sampling scale of $0''.045$ pix⁻¹.

To extract the expansion on the sky of Hen 2–104 these two images need to be brought to exactly the same astrometric grid. This is not possible in this case due to slightly different roll angles and pointings, and possible residuals in the distortion correction done using multidrizzle for the two epochs. We used THELI¹ (Erben et al. 1995) to define an astrometric reference frame based on the stellar sources in the field. Given the small rotation and distortion corrections, the images were then resampled to the new grid, using the coordinates of the central star of Hen 2–104 as the reference projection point. The relative astrometric accuracy between the two images was approximately 0.2 pixel.

2.2. Integral field spectroscopy

Integral-Field Spectroscopy was obtained at Kueyen, Telescope Unit 2 of the 8 m VLT at ESO’s observatory on Paranal, on April 2, 2004. The inner lobes of the nebula were covered by the ARGUS IFU at PA = 122° using the lowest spatial resolution (314 fibres each with a size of $0''.52$ projected onto the sky, giving a total of $11''.4$ by $7''.3$ field of view). Two 300 s exposures were taken with the H679.7 grating, covering the region between 660 and 690 nm, and then co-added. The resolving power was $R = 30\,000$, corresponding to a line *FWHM* of 10.5 km s⁻¹. The seeing was $0''.7$. The VLT data were kindly reduced by Reinhard Hanuschik using the ESO pipeline, and then further analysed using standard IRAF routines.

2.3. Near-infrared spectroscopy

A 120 s near-IR spectrum of the core of Hen 2–104 was taken with SOFI at the ESO New Technology Telescope (NTT) on May 2, 2004, in the 0.95–2.5 μ m range, with a resolving power of $R = 930$ for a slit width of $0''.6$. The spectrum was reduced following standard IRAF procedures.

3. An improved spatio-kinematical modelling

The image of the nebula surrounding Hen 2–104 is shown in Fig. 1. It consists of two pairs of nested, emitting gas lobes. According to Corradi et al. (2001), the two pairs of lobes are likely coeval, and not the result of two similar consecutive outbursts (with the inner lobes being a younger version of the outer ones) since their expansion velocities are (dramatically) different, and their kinematical ages are very similar. The polar jets of the nebula are also roughly coeval with the inner and outer lobes. The inner lobes show latitude-dependent surface brightness variations, which produce the systems of ellipses observed in the HST images (Corradi et al. 2001). The outer lobes, on the other hand, appear fragmented by Kelvin-Helmholtz instabilities into a myriad of clumpy and filamentary structures. Most of them, specially in the furthest regions, have outward-facing tails (see Contini & Formigini 2001; González et al. 2005).

We used the VLT IFU to map the 2-D distribution and Doppler shifts of the emission from the core and the whole inner lobes. The core shows a bright He I $\lambda 667.8$ emission line, which is also visible throughout the inner nebula. The [SII] $\lambda 671.7, 673.1$ emission lines present a high S/N ratio over the whole inner lobes, while are somewhat weaker in the portion of the outer lobes contained in the small field of view of the IFU. This, together with a wavelength dispersion sufficiently large to separate the emission from the two systems of lobes wherever

¹ ftp.ing.iac.es/mischa/THELI/

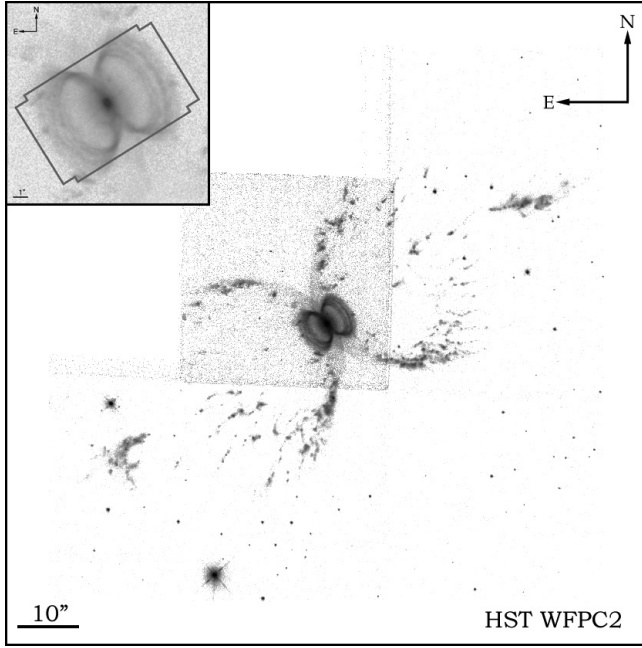


Fig. 1. The HST $F658N$ image of the nebula of Hen 2–104 obtained in 2003. The ARGUS IFU unit covering the inner lobes is overlaid on the *top-left* zoomed region.

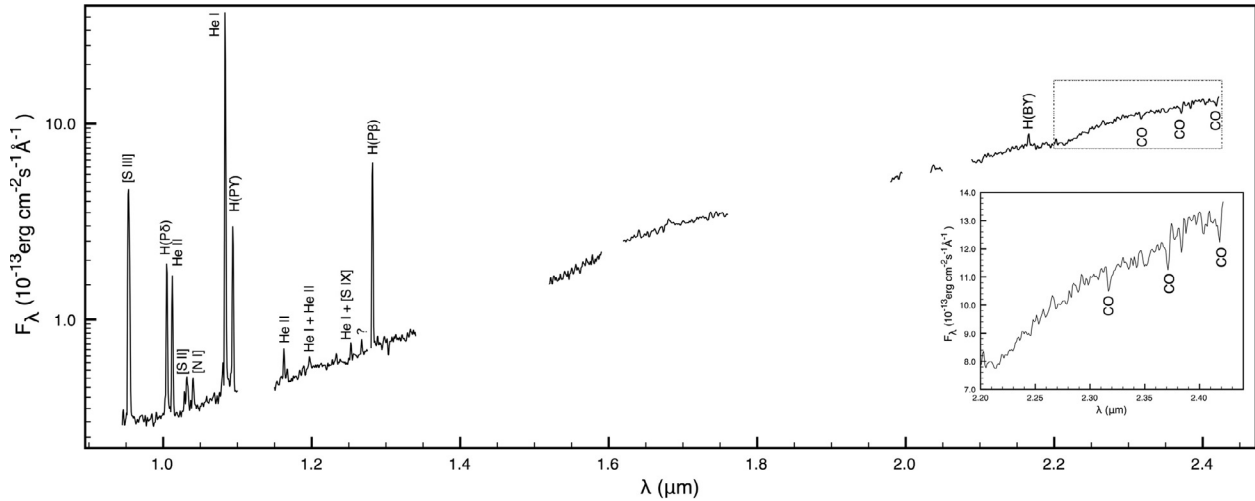


Fig. 2. NTT+SOFI NIR spectrum of the core of Hen 2–104. Regions within which telluric absorption bands severely degraded the spectrum have been removed. *Right bottom:* magnification of the region spanning from 2.2 to 2.45 μm .

their respective radial velocities differ in more than 40 km s^{-1} , enables a 3-D analysis of the two structures separately to be completed.

The IFU [SII] 22×14 fiber-array was rearranged in columns and rows to construct a grid of pseudo long-slit spectra, with length $11''.4$ and $7''.28$ respectively, and slit width $0''.52$. A spatio-kinematical model was then built and fit to the spectral data and the shape of the inner lobes and base of the outer lobes in the [NII] HST image (see Santander-García et al. 2004, for a detailed description of the method). An analytical description assuming axial symmetry and using the formula in Solf & Ulrich (1985) was adopted, for a surface, described in spherical coordinates by:

$$r = tD^{-1}[v_{\text{equator}} + (v_{\text{polar}} - v_{\text{equator}}) \sin |\theta|^\gamma]$$

where r is the apparent distance to the central source, tD^{-1} is the kinematical age of the outflow per unit of distance to the nebula, v_{polar} and v_{equator} are the velocities of the model at the pole and equator respectively, θ is the latitude angle of the model, and γ is a dimensionless shaping factor. This assumes that each gas

particle travels in the radial direction from the central star with a velocity proportional to its distance from the central source. For the inner lobes, emission is restricted to latitudes that correspond to the observed system of ellipses. In both cases, the resulting two-dimensional model was scaled to fit the size of the object, rotated around the symmetry axis to produce a three-dimensional figure, and inclined to the plane of the sky. The resulting geometrical shape and velocity field is used to generate simplified model images and velocity plots for direct comparison with the real image and spectra.

The fit to the data is performed by allowing the different parameters of the model to vary over a large range of values and visually comparing each resulting model to the image and spectra, until the optimal model is found. The results are shown in Figs. 3–6 and the corresponding parameters in Tables 1 and 2.

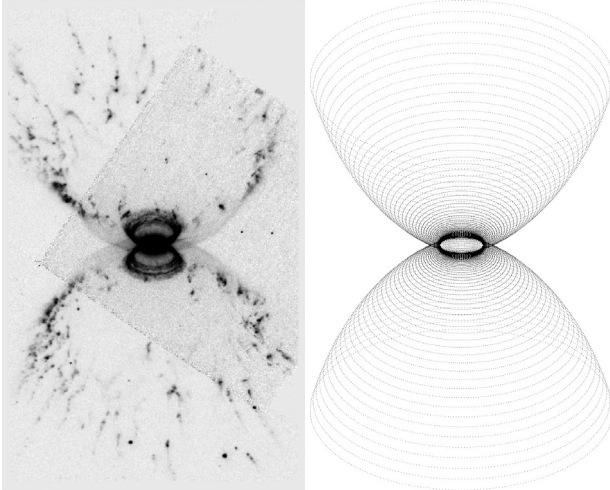
Almost all emission from the inner lobes, both in the [NII] image and the [SII] spectra, was found to be faithfully accounted for by a series of rings inscribed on the walls of a truncated Solf & Ulrich (1985) model at the highest latitudes, from 25°

Table 1. Best-fitting parameters for the outer lobes of Hen 2–104.

Parameter	Value	Range
tD^{-1} (yrs kpc $^{-1}$)	1300	(1200–1400)
v_{polar} (km s $^{-1}$)	230	(210–250)
v_{equator} (km s $^{-1}$)	12	(8–15)
γ	3.2	(2.8–3.8)
θ_{max} (°)	52	(50–53)
i (°)	58	(56–60)

Table 2. Best-fitting parameters for the inner lobes of Hen 2–104.

Parameter	Value	Range
tD^{-1} (yrs kpc $^{-1}$)	1100	(900–1300)
v_{polar} (km s $^{-1}$)	90	(210–250)
v_{equator} (km s $^{-1}$)	11.3	(7–15)
γ	4.5	(3.5–5.0)
θ_{min} (°)	25	(24–27)
θ_{max} (°)	39	(37–40)
i (°)	58	(56–62)

**Fig. 3.** Left: the [NII] HST image of the inner and outer lobes of Hen 2–104. Right: adopted model of the outer lobes.

to 39°, which expand at a maximum velocity of ~ 25 km s $^{-1}$. The outer lobes, on the other hand, were found to share the symmetry axis of their smaller counterpart, $58 \pm 2^\circ$ inclined with respect to the line of sight, and with a similar, within uncertainties, age of the nebula. We therefore confirm the overall results of Corradi et al. (2001), while refining the value of the fitting parameters for the inner lobes thanks to the complete coverage of this region of the nebula by the ARGUS IFU. A systemic velocity $v_{\text{LSR}} = -85$ km s $^{-1}$ was derived, in agreement with the measurement of Corradi & Schwarz (1993a).

4. The distance

The distance to the nebula of Hen 2–104 was determined by means of its expansion parallax. The apparent expansion in the plane of the sky was calculated between two images taken at two different epochs. To measure the nebula distance, this apparent expansion was then combined with a three-dimensional model of the expansion pattern, which was recovered from the analysis of the images and the radial velocity field.

The apparent expansion of both the outer lobes and polar jets of Hen 2–104 can be observed immediately by blinking the aligned 1999 and 2003 HST images. The amount of expansion of the outer lobes and jets was quantified in two different ways (Reed et al. 1999): 1) by deriving the growth of the entire outer lobes and jets using the so-called magnification method; and 2) by calculating the expansion of several individual knots by applying cross-correlation methods to the corresponding surface brightness radial profiles.

4.1. Expansion parallax via the magnification method

A residual image of the nebula was obtained by subtracting the 1999 image from the 2003 one, after the images had been registered and aligned with respect to the central core. A generalized pattern can be seen in the jets and edges of the outer lobes, with positive residuals on the outside and negative ones on the inside, indicating the expansion of the nebula in the period from 1999 to 2003.

To quantify the growth of the nebula, we determined the magnification factor, M , that had to be applied to the 1999 image, to minimize the rms of the residual image obtained by subtracting the magnified image created from the 2003 image. In practice, however, the complex structure of the nebula, the evolution of the brightness and shape of individual knots, and the small, non-radial components of movement of each knot (Rayleigh-Taylor instabilities, diffusion into the medium, etc.) complicate the analysis.

Each jet, in addition to two well-exposed regions of the outer lobes (see Fig. 7), were independently analysed. The minimum rms of the residual images of the Northwest and Southeast jets were found to correspond to magnification factors M equal to 1.0009 and 1.0010 respectively; both with an uncertainty of ± 0.0002 . On the other hand, the M factors that minimized the residual images of the Northwest and Southeast regions of the outer lobes were 1.0008 and 1.0012 respectively, while the uncertainty in these cases was ± 0.0003 . Independent comparisons of the residual images by eye confirmed all these results. Thus, the growth of both the jets and outer lobes is uniform, within the errors, with average values of $M = 1.00095 \pm 0.00020$ and $M = 1.00100 \pm 0.00030$, respectively.

Given the magnification factor M for the jets and outer lobes, and the kinematical age-distance parameter tD^{-1} (1300 yrs kpc $^{-1}$ for the outer lobes, from Table 2, and 1200 yrs kpc $^{-1}$ for the jets, Corradi et al. 1993a), the expansion parallax can be determined by comparing the amount of growth of each feature in time between 1999 and 2003, t_B , with the features' kinematical age. Hence:

$$D(\text{kpc}) = \frac{t_B(\text{yrs})}{(M - 1) tD^{-1}(\text{yrs kpc}^{-1})}.$$

We found that the magnification method applied to the jets and outer lobes of Hen 2–104 provides consistent values of $D_{\text{jets}} = 3.5 \pm 0.7$ kpc and $D_{\text{outerlobes}} = 3.1 \pm 0.9$ kpc, respectively.

4.2. Expansion parallax via radial-profile method

While not providing a global, intuitive vision of the growth of the nebula and of deviations from pure radial expansion, the method that involves the study of radial profiles enables the radial expansion of individual features to be traced.

This procedure analyses the one-dimensional surface brightness radial profiles that pass through a given bright and sharp

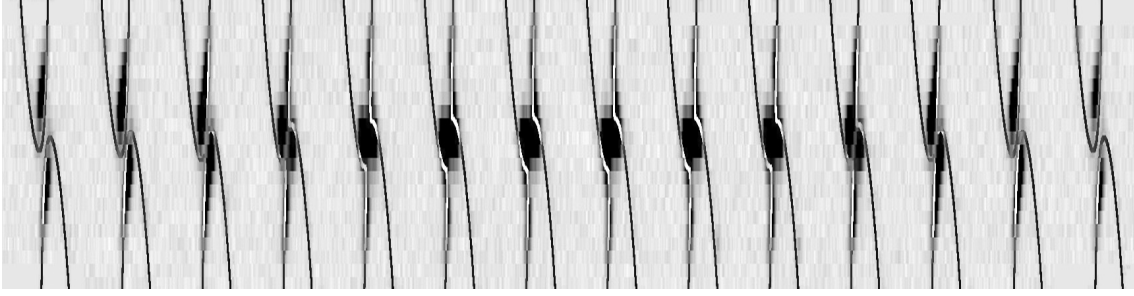


Fig. 4. The ESO [SII] ARGUS IFU spectra rearranged so as to simulate long-slit spectra at PA = 122° (long axis of the nebula), and offset from −3′38 (SW) to +3′38 (NE) from left to right, in increments of 0′52. The spatio-kinematical model of the outer lobes has been superimposed. Each frame is 10′92 tall and 260 km s^{−1} wide. Southeastern side is up.

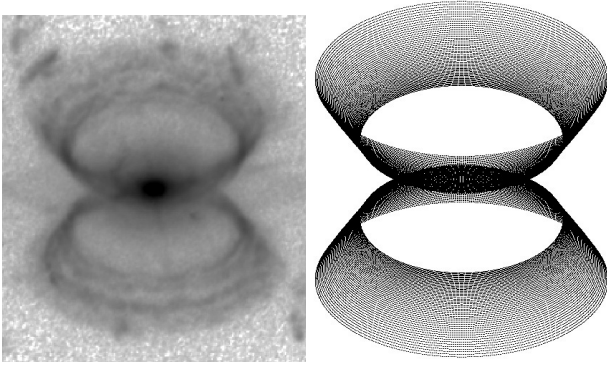


Fig. 5. *Left:* the [NII] HST image of the inner lobes of Hen 2–104. *Right:* adopted model of the inner lobes.

knot. Ideally, any profile from the 2003 image will be similar to the one from 1999, except that the feature will be shifted outwards. To measure the angular expansion $\dot{\theta}$ of the feature in the plane of the sky, the 1999 and 2003 profiles are cross-correlated.

Figure 8 shows the angular expansion $\dot{\theta}$ (in milliarcseconds) of 45 well-defined knots chosen in the outer lobes and jets.

Assuming pure radial motion of the features, the distance to the nebula is computed by comparing the angular expansion of each knot to its velocity in the plane of the sky:

$$D(\text{kpc}) = 0.211 \frac{v_{\text{sky}}(\text{km s}^{-1})}{\dot{\theta}_{\text{mas yr}^{-1}}}.$$

For each knot in the jets, its radial velocity measured using the major axis spectrum at PA = 122° from Corradi et al. (2001), was combined with the expansion in the plane of the sky derived from the cross-correlation of the radial profile. The inclination was assumed to be similar for the inner and outer lobes (Sect. 3). For the outer lobes, the velocity in the plane of the sky was computed using the spatio-kinematical model in Sect. 3.

After averaging the results for all the knots in the outer lobes, we obtained $D_{\text{outerlobes}} = 3.1 \pm 1.0$ kpc, and $D_{\text{jets}} = 3.4 \pm 1.0$ kpc for the knots in the jets.

The distance found using radial fitting is therefore fully consistent with that derived using the magnification method; in the following, we adopt an average distance of $D_{\text{Hen 2–104}} = 3.3 \pm 0.9$ kpc. We note the considerable size of the nebula at this distance, amounting to ~ 2.0 pc, and the large kinematical ages of the inner and outer lobes, which would be 3700 ± 1200 , and 4200 ± 1200 years, respectively.

5. The NIR spectrum

The NIR spectrum of the core (see Fig. 2) shows a variety of emission lines over an almost featureless rising continuum.

The region between 0.95 and 1.3 μm shows Hydrogen and Helium atomic recombination lines, in addition to [SII], [SIII], [NI], and H₂. The region redward of 2.1 μm shows three CO absorption bands that are typical of late AGB stars (e.g. Kamath & Ashok 2003). These bands, although barely visible in the dominant continuum produced probably by hot circumstellar dust, show for the first time some photospheric spectral features of the Mira in the system, which has only been indicated to date by its characteristic NIR photometric light curve (Whitelock 1987).

The emission lines and absorption band CO identifications are shown in Table 3.

The featureless NIR continuum of Hen 2–104 is quite peculiar for symbiotic stars (cf. Whitelock 2003), where in general this part of the spectrum is dominated by deep absorption bands of the red giant. We note that Mz 3 and M 2–9, two nebulae suspected of having a symbiotic binary nucleus, have similar spectra. It is likely that the rising continuum is emission produced by a significant amount of hot circumstellar dust, but a detailed modelling of the spectrum is beyond the scope of this paper. What is instead relevant to the present discussion, is the fact that it is clear that the emission in the *K*-band is not always a good measure of the luminosity of the red giant of the system; distances computed by the Mira period-luminosity relationship using the *K* magnitude, are therefore probably affected by large uncertainties.

6. Nebular density and mass

6.1. Density map

The integral-field spectroscopy data, featuring the [SII] $\lambda\lambda 671.7, 673.1$ emission line doublet, enable a density map to be built that covers the entire inner lobes and the base of the outer lobes (Fig. 9). As mentioned previously, the large resolving power ($R = 30\,000$) of the spectra was sufficiently high to separate the inner lobes from the outer lobes wherever their respective radial velocities differed by more than 40 km s^{−1}.

In the absence of actual temperature measurements for the lobes, we assume $T_e = 10\,000$ K for both structures. The resulting densities range from $n_e = 500$ to 1000 cm^{−3} for the inner lobes, and from ~ 300 to 500 cm^{−3} for the base of the outer lobes. The core has the highest measured [SII] densities, $n_e \sim 2400$ cm^{−3}. However, the [SII] lines seen towards the core probably arise in the outer layers of a dense circumstellar envelope, as in the case of other symbiotic Mira HM Sge (Corradi & Schwarz 1999). A core density larger than 2.5×10^6 cm^{−3} is

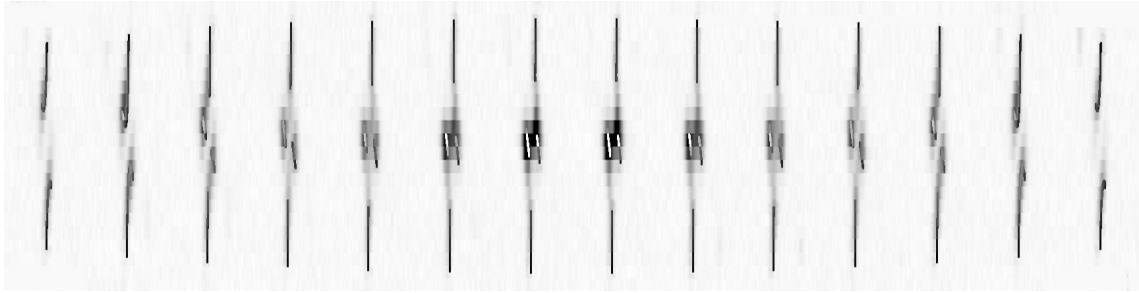


Fig. 6. The ESO [SII] ARGUS IFU spectra arranged in columns along the IFU longer axis. Frames correspond, from left to right, to PA = 122° and offsets from -3'38 (SW) to +3'38 (NE) from left to right, in increments of 0'.52. The spatio-kinematical model of the inner lobes has been superimposed. Note: each frame is 10'.92 tall and 260 km s⁻¹ wide. Southeastern side is up.

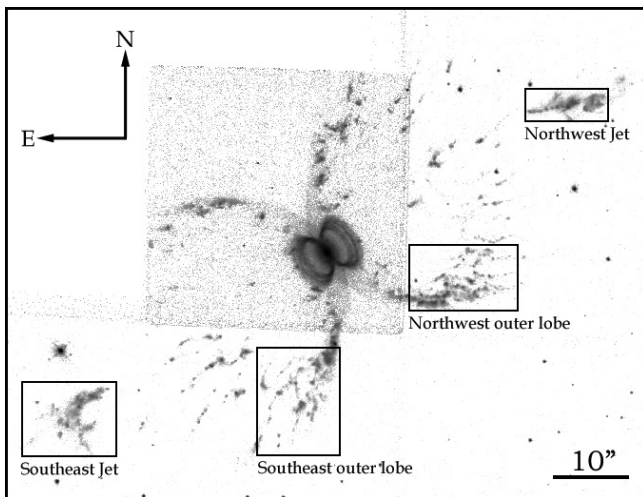


Fig. 7. HST [NII] WFPC2 2003 image. The four regions in which the rms of the magnification method residual image were measured are indicated by the black boxes.

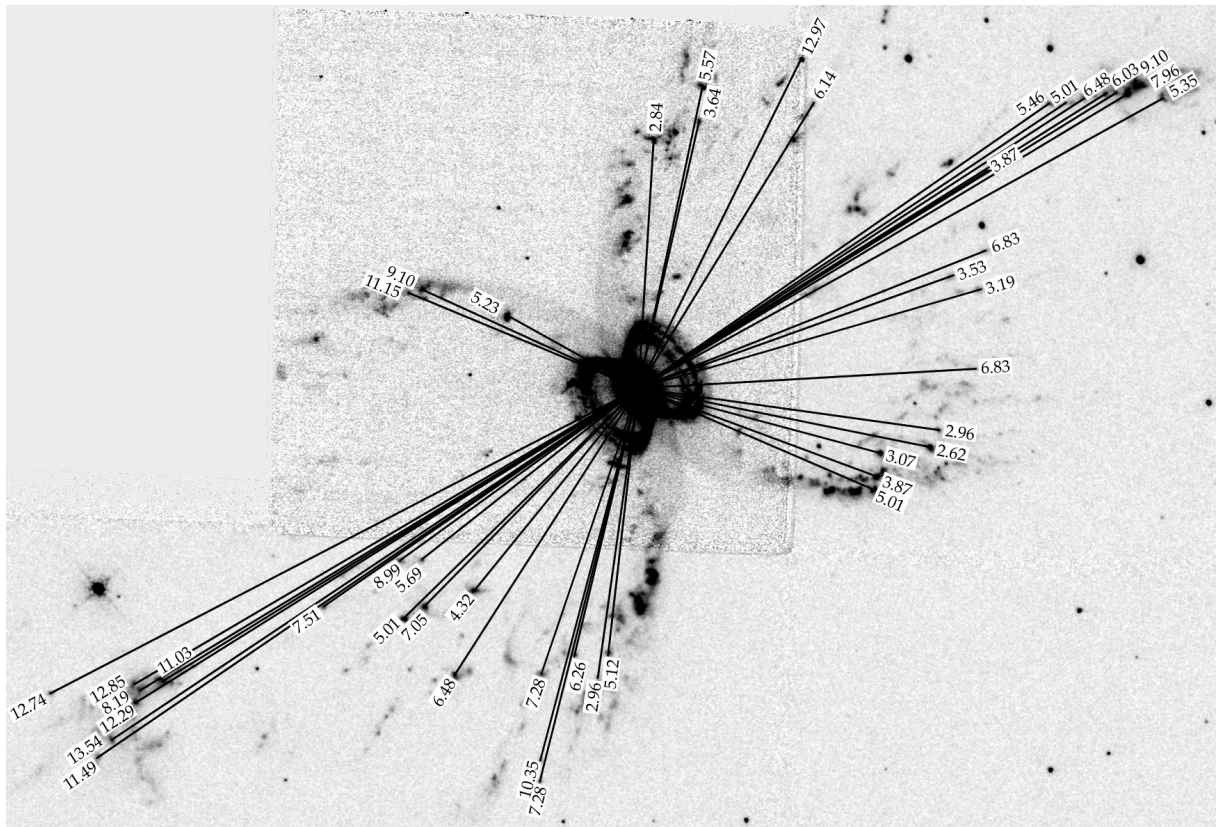


Fig. 8. HST [NII] WFPC2 2003 image along with the radial expansion (in mas yr⁻¹) of the knots of the outer lobes and jets analyzed in Sect. 3.

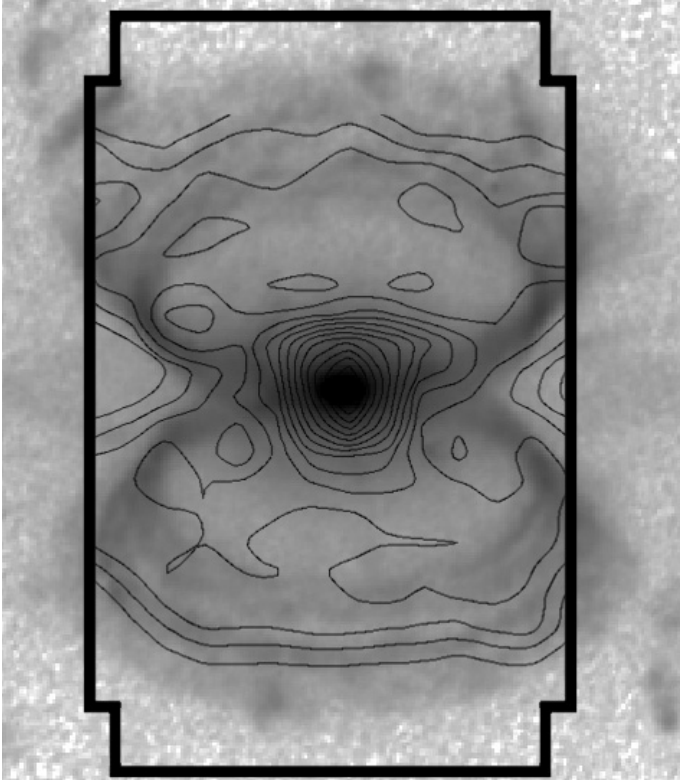


Fig. 9. Density map of the inner lobes and base of the outer lobes of Hen 2–104. The contour levels span from $n_e = 200$ to 3000 cm^{-3} with step 200.

estimated for Hen 2–104 from the [OIII] lines (Freitas Pachecho & Costa 1996). At these densities, the [SII] lines are collisionally quenched. These results confirm those given by Corradi & Schwarz (1993a).

6.2. Ionized mass

The ionized mass of the nebula around Hen 2–104 can be estimated using the formula

$$M_{\text{H}^+} = \frac{m_{\text{H}} F(\text{H}\beta) 4\pi D^2}{h\nu_{\beta} \alpha_{\text{B}}^{\text{eff}} n_e}$$

where D is the distance, n_e is the nebular electron density, $F(\text{H}\beta)$ is the total $\text{H}\beta$ flux, m_{H} is the mass of the hydrogen atom, $h\nu_{\beta}$ is the energy of an $\text{H}\beta$ photon, and $\alpha_{\text{B}}^{\text{eff}}$ is the effective recombination coefficient for case B (adopted from Osterbrock 1989). After correcting the observed $\text{H}\alpha$ flux for an extinction of $A_{\text{v}} = 3.0$ mag (average of the values found by Lutz et al. 1989 and Freitas Pacheco & Costa 1996), and applying the theoretical $\text{H}\alpha$ to $\text{H}\beta$ ratio of 2.85 (for an electron temperature of 10 000 K), we obtain $F(\text{H}\beta) = 1.3 \times 10^{-11} \text{ erg cm}^2 \text{ s}^{-1}$. Assuming an average density of 500 cm^{-3} and the distance found in this work, we compute an ionized mass of $\sim 0.16 M_{\odot}$. The extinction correction is very important in the above calculation; if we instead assume an interstellar extinction of 1.6 mag, as derived from the Galactic extinction model by Drimmel et al. (2003) for the location of Hen 2–104 and the computed distance, the resulting ionized mass is $0.05 M_{\odot}$. These values have to be considered as lower limits, because they neglect local extinction due to dust around and inside the nebula.

A different mass estimate can be obtained by computing, both for the inner and outer lobes, the volume of each feature

Table 3. Hen 2–104: NIR emission line and absorption-band identification, along with their fluxes and associated errors, which include both the Poissonian error and the error in the determination of the continuum. “?” denotes that the line was unidentified.

λ_0 (laboratory) (Å)	Element (emission)	Flux ($10^{-13} \frac{\text{erg}}{\text{cm}^2 \text{ s}}$)	error (%)
9463.61	He I $3^3\text{S}-5^3\text{P}^0$	2.11	14
9532.55	[SIII]	106.0	1
10 027.73	He I $3^3\text{D}-7^3\text{F}^0$	0.7	17
10 049.37	H(P δ)	28.6	1
10 123.61	He II $4-5$	23.1	1
10 286.5	[SII]	1.32	10
10 320.3	[SII]	4.83	7
10 370.5	[SII]	0.44	20
10 397.7+10 398.2	[Ni]	3.62	7
10 830.2	He I	640.0	1
10 912.0	He I	1.85	18
10 938.1	H(P γ)	44.9	1
11 626.2	He II $5-7$	3.85	10
11 673.24	He II $6-11$	1.17	31
11 970.0	He I+He II	2.19	36
12 329.0	H ₂ (3,1)S(1)	1.8	18
12 528.0	He I	2.67	10
12 673.	?	2.3	10
12 785.0	He I	5.2	7
12 818.08	H(P β)	97.0	1
16 407.19	H(Br12)	6.98	39
16 806.52	H(Br11)	10.2	52
21 655.29	H(Br γ)	28.9	15

λ (bandhead) (μm)	Molecule (absorption)	Flux ($10^{-13} \frac{\text{erg}}{\text{cm}^2 \text{ s}}$)	error (%)
2.32	CO	0.34	28
2.37	CO	0.35	46
2.42	CO	0.59	27

occupied by gas in the following manner. As the geometry of the surface of the lobes is known from our spatio-kinematical modelling (Sect. 3), and the electron-density distribution is also known from the [SII] line ratio, the only other parameter needed to compute the volume occupied by the emitting gas is the thickness of the walls of the lobes, if the filling factor (cf. Pottasch 1984) is assumed to be about unity. Three-dimensional models with different thicknesses were produced using IDL (RSI) routines adapted from the VISNEB tools developed for the Cloudy 3D code (Morisset 2006). A cubic grid of 300^3 cells was used to generate and rotate a 3D emissivity model, with an emissivity per unit volume $\propto n_e^2$. The emission along the line of sight was then integrated to generate a synthetic image for collisionally-excited lines, assuming that the ionic abundance and electron temperature are constant throughout the lobes. This procedure was repeated several times to allow the thickness of the 3D model to vary over a wide range.

To find the optimal thickness that accounts for the observed inner and outer lobes, residual images were obtained by subtracting each synthetic image from the real HST one. The regions around the edges of each lobe (i.e. where the walls of the structure are perpendicular to the plane of the sky and therefore its thickness is easier to estimate) were analysed in the residual images, both by visual comparison and by measuring the rms of each region. Illustrative samples of these synthetic images, both for the outer and inner lobes, are shown in Figs. 10 and 11. The resulting best-fit thickness was $0'.9 \pm 0'.4$ and $3'.4 \pm 0'.5$, for the inner and outer lobes respectively. Finally, to account for the

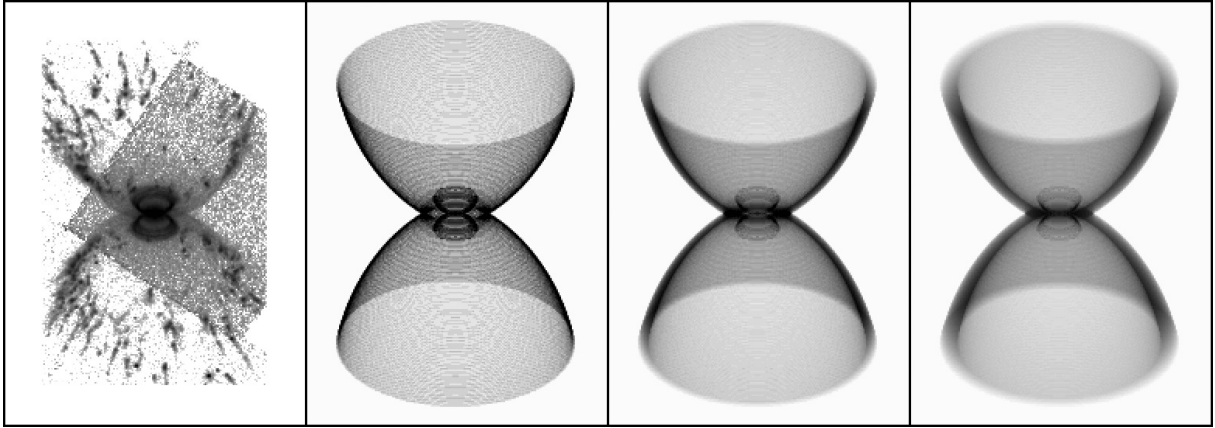


Fig. 10. From left to right: HST [NII] image from 2003 and illustrative sample of synthetic images of the nebula. The thickness of the outer lobes of the three models are $1''.0$, $3''.5$ and $6''.0$, respectively, while the inner lobes show a constant thickness of $0''.9$.

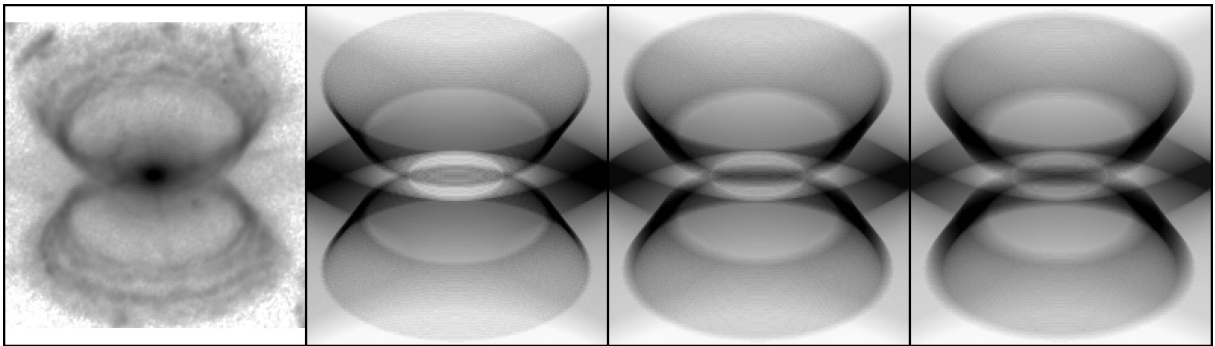


Fig. 11. From left to right: HST [NII] image from 2003 and illustrative sample of synthetic images of the inner lobes (and the central region of the outer ones). The thickness of the inner lobes of the three models are $0''.4$, $0''.9$ and $1''.4$, respectively, while the outer lobes show a constant thickness of $3''.5$.

knotty appearance of the outer lobes, we computed the fraction of the total volume of the model occupied by gas. The procedure to do this was to count the number of pixels in the HST images whose surface brightness was larger than 3 times the statistical noise of the background, and compute which fraction of the area projected on the sky of the model nebula was effectively filled. The result was that 0.34 ± 0.06 of the total volume of the outer lobes is filled by gas.

Therefore, using typical densities of $n_e = 600 \text{ cm}^{-3}$ and $n_e = 350 \text{ cm}^{-3}$ for the inner and outer lobes, respectively, and assuming a roughly solar abundance for the nebula, the resulting ionized masses for the two pairs of lobes are $(4.6 \pm 0.9) \cdot 10^{-3}$ and $0.08 \pm 0.01 M_\odot$, respectively, for a total of roughly $\sim 0.1 M_\odot$ for the entire nebula. This value is midway between, but broadly consistent with, the two previous estimates of 0.16 and $0.05 M_\odot$ which were obtained by varying the adopted extinction, and clearly implies a relatively large mass for the nebula.

7. Discussion

Schwarz et al. (1989) discovered the extended nebula around Hen 2–104, and they would probably have classified it as a planetary nebula, had Whitelock (1987) not found, two years before, a long-period pulsation of the central star by means of NIR photometric monitoring. In fact, apart from indirect hints suggesting a symbiotic nature (e.g. a high density core, NIR colours unusual for a PN, and an articulated high-excitation spectrum), this was the only evidence for the presence of a cool giant. The NIR spectrum presented in Sect. 5 shows for the first time the

spectral signature of the red giant in the spectrum. However, a strong featureless continuum, presumably from hot circumstellar dust, renders these bands barely visible. Thus, given the difficulties of direct detection of the Mira in some genuine symbiotic nebulae such as Hen 2–104, the already long debate on the nature of some bipolar nebulae with dust-dominated NIR spectra and high-density compact cores (e.g. Mz 3 and M2-9, see Schmeja & Kimeswenger 2003; Phillips 2007; Santander-García & Corradi 2007b) is not a surprise.

In this work, we derive a distance for Hen 2–104 of 3.3 ± 0.9 kpc by means of the expansion-parallax method. It is known that the expansion-parallax determinations can be affected by shocks. This is, for example, the case for the symbiotic Mira Hen 2–147, in which Santander-García et al. (2007a) found that distance is underestimated if shocks are not properly taken into account. The main evidence for shocks in that nebula are the broad and asymmetrical line profiles, which amount to up to 200 km s^{-1} full width at zero intensity (cf. Hartigan et al. 1987). This is not the case for Hen 2–104, where line widths in the jets and lobes are of the order of $\sim 15 \text{ km s}^{-1}$, only slightly larger than the gas thermal-broadening. We therefore conclude that shocks do not strongly affect the expansion-parallax determination of Hen 2–104, as also suggested by the consistent distance estimate for the lobes and the jets, since shocks would a priori act differently on the two components². We consider our expansion-parallax determination to be more robust than the

² Note, however, that even if the actual distance were somewhat larger, the conclusions below would still hold, as the ionized mass would increase accordingly.

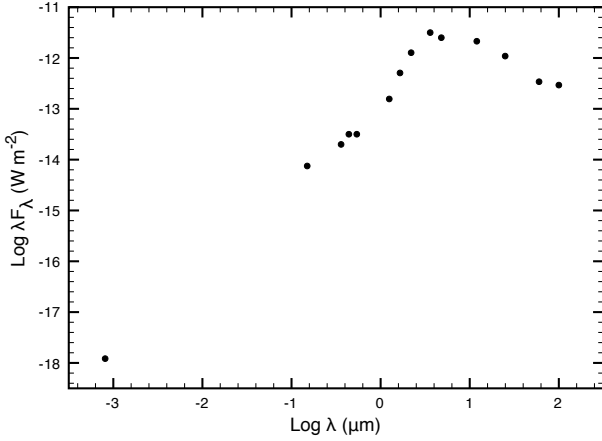


Fig. 12. Observed spectral energy distribution of Hen 2–104, from 1.2 Å to 100 μm, based on the values quoted in Schwarz et al. 1989 for the UVB and the IR photometry, the IRAS fluxes, the IUE UV fluxes and the Chandra X ray fluxes.

distance obtained using the period-luminosity relationship for the Mira (Whitelock 1987), because our spectra show that the K -band magnitude does not provide a reliable measure of the luminosity of the Mira.

Application of the period-luminosity relation (Feast et al. 1989; Groenewegen & Whitelock 1996; and Whitelock et al. 1994) to the Mira of Hen 2–104 ($P = 400$ days, Whitelock 1987), would imply a bolometric luminosity for the AGB star of $\sim 6000 L_{\odot}$. This can be compared with the total luminosity of the system derived from the spectral energy distribution presented in Fig. 12, at the computed distance of 3.3 kpc. From the latter, to obtain a luminosity larger than $6000 L_{\odot}$, where the luminosity of the white dwarf companion should also be considered, the interstellar extinction must be $A_v > 2.9$ mag. This value is significantly larger than that obtained using the Galactic model by Drimmel et al. (2003, see Sect. 6.2), and closer to the determinations of Lutz et al. (1989), $A_v = 2.23$ mag, and Freitas Pacheco & Costa (1996), $A_v = 3.7$ mag.

Another result of this work that deserves discussion is the remarkable ionized mass of the extended nebula, amounting to about a tenth of a solar mass (see Sect. 6.2). Given such a large value, and considering that only a negligible fraction of the Mira wind is captured by the white dwarf, it seems clear that the main donor of mass for the nebula is the Mira. As Corradi et al. (2001) suggested, this kind of nebulae is likely to be the result of the interaction of the slow winds from the Mira with the fast winds from an outbursting white dwarf. Given the articulated structure of these nebulae, it is not easy to understand how the different winds contribute to each morphological component, but it seems natural to associate the high velocity features (such as the polar jets) directly with the fast winds from the hot white dwarf and its accretion disc. Many of the features of the nebula around Hen 2–104 could be explained by the weak-jet model of the hydro-dynamic calculations by García-Arredondo & Frank (2004). Although the initial conditions that these authors assumed for the two case studies were different, the conclusions of their model are applicable. This emphasizes the key role of the Mira in supplying the material and the essential role of the white dwarf companion in accelerating and, in all probability, deflecting the streamlines of the Mira’s wind to shape the bipolar morphology that we see today. Our spatio-kinematic fit clearly shows that the outflow speeds are slowest at low latitudes and highest along the polar direction. This is similar to the pattern

found in most bipolar PNe (e.g. Corradi 2004), as well as in other classes of objects such as the homologously-expanding bipolar homunculus of η Carina (Smith & Gehrz 1998). Thus, the mechanisms that may have formed Hen 2–104 are not limited to symbiotic stars and PNe, and may be common when the mass loss rate of the source is high.

We have also found that the walls of the two lobe pairs of Hen 2–104 are very thin compared to their radial distance from the star. A comparison to the sound crossing time allows for some speculation about the mechanism holding the walls tightly together. If the gas temperature is (and has been) 10^4 K since the ejection ~ 4000 yrs ago (at the computed distance), the sound speed is 10 km s^{-1} , so it travels 1.2×10^{12} km in 4000 yrs. The wall thickness of the inner lobes ($0''.9$), 3.5×10^{11} km, is less than the sound travel distance, implying that something like an outside pressure or an embedded magnetic field is holding the walls of the inner lobes together, perhaps accounting for their relatively smooth and structured appearance and high emission density. The outer walls are 1.3×10^{12} km thick ($3''.4$), which is roughly the sound crossing distance. This means that the walls of the outer lobes are expanding at their sound speed (i.e. driven by their own thermal pressure).

For a typical AGB wind speed of $\sim 15 \text{ km s}^{-1}$ (Habing, et al. 1994), it would take $\sim 2.6 \times 10^4$ yrs for the gas lost by the Mira of Hen 2–104 to fill the volume presently occupied by the inner and outer lobes of the nebula (~ 0.4 pc in radius at the adopted distance). During this time, an average mass loss rate of $\sim 3.5 \times 10^{-6} M_{\odot} \text{ yr}^{-1}$ would be needed to accumulate the total mass of the nebula ($\sim 0.1 M_{\odot}$) around the system, that later would be shaped by fast winds from the outbursting white dwarf companion. This mass loss rate is in good agreement with that expected from a $6000 L_{\odot}$ Mira variable (Alard et al. 2001), making the depicted scenario a coherent one and reinforcing our distance and mass estimates.

In any case, the mass of the nebula of Hen 2–104 is remarkably larger than previously thought for this class of objects, and more similar to the ionized masses of genuine PNe (Pottasch 1984). Thus the Mira in Hen 2–104 would be in a quite evolved stage, close to the tip of the AGB, where due to strong mass loss a massive circumstellar envelope can be built up. The ionized nebula that we observe can therefore be seen as a sort of “premature” PN, in which the nebular shaping and excitation is done by the WD companion, which “anticipates” the post-AGB evolution of the Mira. We note that the kinetic energy of the nebula of Hen 2–104 ($\sim 8 \times 10^{44}$ erg) and its momentum ($\sim 10^{39} \text{ g cm s}^{-1}$) are similar to those of regular PNe, and significantly lower than the momentum computed by Bujarrabal (2001) for a number of multi-polar young and proto-PNe. The energetics of the outflow of Hen 2–104 can be accounted for by the Mira luminosity and the energy released by a slow-nova explosion on the WD companion.

In the past, it has often been stated that a distinctive characteristic of the nebulae around symbiotic stars is that they are one or two orders of magnitude less massive than PNe. Hen 2–104 shows that this is not the rule, so that the line dividing PNe from symbiotic nebulae might actually be more blurred than previously thought.

Acknowledgements. The authors wish to thank Vera Kozhurina-Platais, Warren Hack, Anton Koekemoer, and Richard Hook from STScI for their kind help in multidrizzle usage, Reinhard Hanuschik for the FLAMES dataline processing, and the anonymous referee for their comments and suggestions which improved the paper.

References

- Alard, C., Blommaert, J. A. D. L., Cesarsky, C., et al. 2001, *ApJ*, 552, 289
- Bujarrabal, V., Castro-Carrizo, A., Alcolea, J., & Sánchez-Contreras, C. 2001, *A&A*, 377, 868
- Contini, M., & Formigini, L. 2001, *A&A*, 375, 579
- Corradi, R. L. M. 2003, in *Symbiotic stars probing stellar evolution*, ed. R. L. M. Corradi, J. Mikolajewska, & T. J. Mahoney, *ASP Conf. Ser.*, 303, 393
- Corradi, R. L. M. 2004, in *Asymmetrical Planetary Nebulae III: Winds, Structure and the Thunderbird*, ed. M. Meixner, J. H. Kastner, B. Balick, & N. Soker, *ASPC*, 313, 148
- Corradi, R. L. M., & Schwarz, H. 1993a, *A&A*, 268, 714
- Corradi, R. L. M., & Schwarz, H. 1993b, *A&A*, 269, 462
- Corradi, R. L. M., & Schwarz, H. 1995, *A&A*, 293, 871
- Corradi, R. L. M., Ferrer, O. E., Schwarz, H. E., Brandi, E. & GarcŚí a, L. 1999, *A&A*, 348, 978
- Corradi, R. L. M., Livio, M., Balick, B., et al. 2001, *ApJ* 553, 211
- García-Arredondo, F., & Frank, A. 2004, *ApJ*, 600, 992
- Drimmel, R., Cabrera-Lavers, A., & López-Corredoira, M. 2003, *A&A*, 409, 205
- Erben, T., Schirmer, M., Dietrich, J. P., et al. 2005, *AN*, 326, 432
- Feast, M. W., Glass, I. S., Whitelock, P. A., & Catchpole, R. M. 1989, *MNRAS*, 241, 375
- Freitas Pacheco, J. A., & Costa, R. D. D. 1996, *A&A*, 309, 629
- González, R. F., Raga, A. C., & Steffen, W., *RMxAA*, 41, 443
- Groenewegen, M. A. T., & Whitelock, P. A., *MNRAS*, 281, 1347
- Habing, H. J., Tignon, J., & Tielens, A. G. G. M. 1994, *A&A*, 286, 523
- Hartigan, P., Raymond, D., & Hartmann, L. 1987, *ApJ*, 316, 323
- Kamath, U. S., & Ashok, N. M. 2002, in *Symbiotic stars probing stellar evolution*, ed. R. L. M. Corradi, J. Mikolajewska, & T. J. Mahoney, *ASP Conf. Ser.*, 303, 133
- Kenyon, S. J. 1986, *The Symbiotic Stars* (Cambridge University Press)
- Kenyon, S. J., & Webbink, R. F. 1984, *ApJ* 279, 252
- Koekemoer, A., Fruchter, A., Hook, R., & Hack, W. 2002, *HST Calibration Workshop*, 337
- Livio, M., Prialnik, D., & Regev, O. 1989, *ApJ*, 341, 299
- Luridiana, V., Pérez, E., & Cerviño, M. 2003, *AJ*, 125, 3196
- Lutz, J. H., Kaler, J. B., Shaw, R. A., et al. 1989, *PASP*, 101, L966
- Mellema, G., *A&A*, 2004, 416, 623
- Morisset, C. 2006, in *Planetary Nebulae in our Galaxy and Beyond*, ed. M. J. Barlow, & R. H. Méndez, *Proc. Inter. Astron. Union, Symp.*, 234, 467
- Munari, U., & Zwitter, T. 1997, *A&A*, 318, 269
- Osterbrock D. 1989, *Astrophysics of Gaseous Nebula and Active Galactic Nuclei*, University Science Books, 20 Edgehill Road, Mill Valley, CA 94941
- Palen, S. E., Hajian, A. R., & Balick, B. 2000, *A&AS*, 196, 6101
- Phillips, J. P. 2007, *MNRAS*, 376, 1120
- Pottasch, S. R. 1984, *A study of Late Stages of Stellar Evolution*, *Astrophysics and Space Science Library*, 107
- Reed, D. S., Balick, B., Hajian, A. R., et al. 1999, *AJ*, 118, 2430
- Sahai, R. 2002, *RMxAC*, 13, 133
- Santander-García, M., Corradi, R. L. M., Balick, B., & Mampaso, A. 2004, *A&A*, 426, 185
- Santander-García, M., Corradi, R. L. M., Whitelock, P. A., et al. 2007a, *A&A*, 465, 481
- Santander-García, M., & Corradi, R. L. M., & Mampaso, A. 2007b, in *Asymmetrical Planetary Nebulae IV*, in press
- Schmeja, S., & Kimeswenger, S. 2003, in *Symbiotic stars probing stellar evolution*, ed. R. L. M., Corradi, J. Mikolajewska, & T. J. Mahoney, *ASP Conf. Ser.*, 303, 446
- Schönberner, D., Jacob, R., & Steffen, M. 2005, *A&A*, 441, 573
- Schwarz, H. E., Aspin, C., & Lutz, J. H. 1989, *ApJ*, 344, L29
- Shaw, R. A., & Kaler, J. B. 1989, *ApJS*, 69, 495
- Smith, N., & Gehrz, R. D. 1998, *AJ*, 116, 823
- Sokoloski, J. L. 2002, in *Symbiotic Stars Probing Stellar Evolution*, ed. R. L. M. Corradi et al., *ASP Conf. Ser.*, 303, 202
- Solf, J., & Ulrich, H. 1985, *A&A*, 148, 274
- Whitelock, P. A. 1987, *PASP*, 99, 573
- Whitelock, P. A. 2003, in *Symbiotic stars probing stellar evolution*, ed. R.L.M. Corradi, J. Mikolajewska, & T. J. Mahoney, *ASP Conf. Ser.*, 303, 41
- Whitelock, P. A., Menzies, J., Feast, M., et al., *MNRAS*, 267, 711
- Wright, A. E., & Allen, D. A. 1978, *MNRAS*, 184, 893